



Low-temperature selective catalytic reduction of NO_x with NH₃: Exploring the mechanism of enhancing H₂O tolerance through methylation functionalization and structural regulation in IPAx-Mn-BTC

Kunli Song^a, Jiyuan Hu^a, Peng Lu^b, Dandan Ma^a, Xinya Zhou^a, Jun Li^a, Ting Jiang^a, Lu Li^a, Shangyuan Wu^a, Jian-Wen Shi^{a,*}

^a State Key Laboratory of Electrical Insulation and Power Equipment, Center of Nanomaterials for Renewable Energy, School of Electrical Engineering, Xi'an Jiaotong University, Xi'an 710049, China

^b Guangdong Province Engineering Laboratory for Air Pollution Control, South China Institute of Environmental Sciences, the Ministry of Ecology and Environment of PRC, Guangzhou 510655, China

ARTICLE INFO

Keywords:

Selective catalytic reduction
De-NO_x
Metal-organic frameworks
H₂O tolerance
Methylation

ABSTRACT

In the selective catalytic reduction (SCR) of NO_x with NH₃, it is crucial to design low-temperature de-nitrification (de-NO_x) catalysts with high H₂O tolerance. Here, we developed a type of low-temperature de-NO_x catalyst (IPAx-Mn-BTC) with strong H₂O tolerance through methyl functionalization. In the presence of the optimal catalyst (IPA50-Mn-BTC), the NO_x conversion only decreased from 97% to 90% after introducing 6% H₂O for 6 h at low temperature of 150 °C. The results of in-situ DRIFTS and density functional theory calculations confirm that the de-NO_x reaction process and the generation of intermediate states that occur on the surface of the IPA50-Mn-BTC are not affected by H₂O. The elimination of the small pore size (< 4.3 nm) and the diminished H₂O adsorption energy resulted from methyl functionalization are the key factors behind the improved H₂O tolerance. This work provides a new approach for designing low-temperature de-NO_x catalysts with high H₂O tolerance.

1. Introduction

The selective catalytic reduction of NO_x to N₂ with NH₃ (NH₃-SCR) is a prevalent de-nitrification (de-NO_x) technology employed today [1–3], especially low-temperature (LT) de-NO_x, which can not only avoid the waste of energy caused by reheating flue gas, but also prevent NH₃ from oxidizing to other NO_x at high temperatures. However, there are unsolved bottlenecks in the application of LT de-NO_x. The flue gas usually contains H₂O, and the de-NO_x reaction also generates H₂O, which not only competes with NH₃ and NO_x for adsorption, but also reacts with SO₂ and NH₃ to form ammonium bisulfate. The generated ammonium bisulfate is not easy to decompose at LT and will deposit on the surface of the catalyst, blocking the active sites and pore structure, and preventing the reactant from reaching the active sites, thereby reducing the de-NO_x effectiveness and even deactivating the catalyst. Although many studies have concentrated on enhancing LT de-NO_x activity [4–6] and SO₂ tolerance [7–9], there are few studies focused on improving H₂O tolerance.

The self-assembly of organic ligands and metal ions results in the

creation of three-dimensional porous metal-organic framework (MOF) structures, endowing with distinctive attributes such as a big specific surface area, tunable and highly dispersed active sites, and a modifiable and fully exposed pore structure [10–12]. These unique MOF characteristics have broad applications in photocatalysis [13,14], electrocatalysis [15,16], thermal catalysis [17,18], etc. Especially for NH₃-SCR, a large number of highly dispersed and exposed active sites ensure a high catalytic activity, and the regulation of the pore size can also ensure the improvement of H₂O and SO₂ tolerance. The above characteristics may be able to solve the bottlenecks of poor SO₂ and H₂O tolerance of the catalyst, as well as the difficulty in decomposing the generated ammonium bisulfate in LT de-NO_x. Numerous investigations have been undertaken to explore the utilization of MOFs to de-NO_x. Xie et al. [19] synthesized a series of MOF-74-Mn, which achieved the NO conversion of above 80% at 210–300 °C with good H₂O tolerance of 10% decrease for 5% H₂O introduction. Zhou et al. [20] synthesized Mn-Ce-MOF, whose NO_x conversion was above 80%, and the performance of introducing 100 ppm SO₂ was decreased by 7%, and the performance of introducing 5% H₂O was only decreased by 3%. Our team has prepared a

* Corresponding author.

E-mail address: jianwen.shi@mail.xjtu.edu.cn (J.-W. Shi).

<https://doi.org/10.1016/j.apcatb.2023.123548>

Received 20 September 2023; Received in revised form 12 November 2023; Accepted 20 November 2023

Available online 23 November 2023

0926-3373/© 2023 Elsevier B.V. All rights reserved.

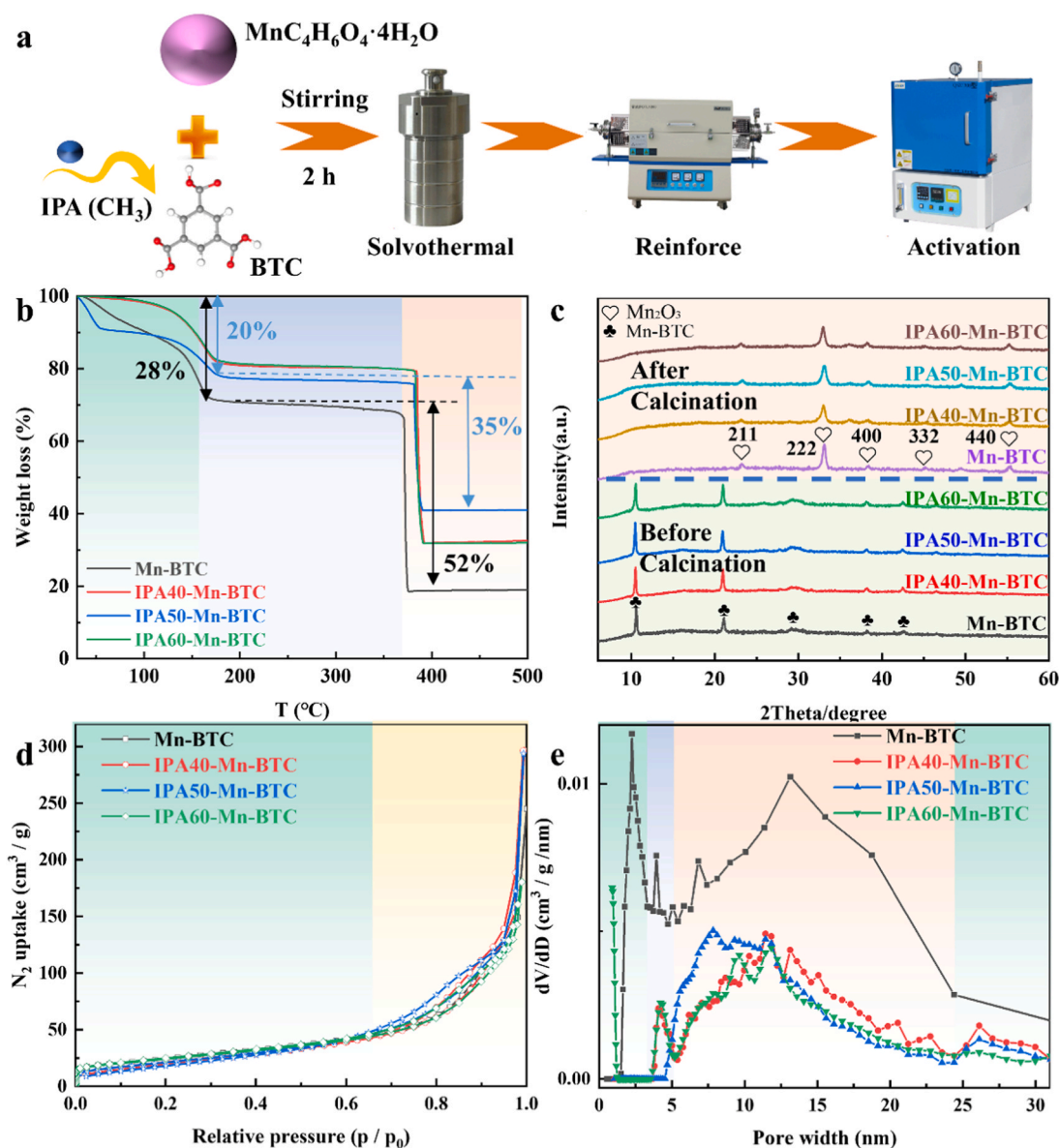


Fig. 1. Catalyst synthesis and characterization: The fabrication illustration of IPAx-Mn-BTC (a); TGA plots of IPAx-Mn-BTC before activation; PXRD patterns of IPAx-Mn-BTC (c); Nitrogen adsorption-desorption isotherms (d) and corresponding pore-size distributions (e).

catalyst, Mn-BTC, with excellent LT de-NO_x performance of above 90% NO conversion at 120–330 °C and high SO₂ tolerance (6% NO conversion decreased with 200 ppm SO₂), but the H₂O tolerance still needs to be improved [21], especially for exhaust gas with high H₂O content.

Adding hydrophobic functional groups is an effective way to improve H₂O tolerance. Li et al. [22] functionalized the FeO/AC de-NO_x catalyst by ammonium persulfate to increase the H₂O tolerance by 20%. Zhu et al. [23] functionalized the TiO₂@HP by methyl to achieve hydrophobic micropores and enhance H₂O tolerance. However, there are few hydrophobic functional groups introduced into MOFs because the introduction of functional groups may affect the coordination process of MOFs and the introduced functional groups may be inert. Therefore, it is also a challenge to introduce hydrophobic functional groups into MOFs to improve the H₂O tolerance of de-NO_x catalysts.

In this study, based on the previous research of Mn-BTC, a series of catalysts, IPAx-Mn-BTC (x is the concentration of IPA), were designed by adding isopropanol (IPA) to the hydrothermal reaction to make the catalysts methylate. Among these developed IPAx-Mn-BTC catalysts, IPA50-Mn-BTC demonstrated the optimal de-NO_x performance (over

90% NO_x conversion within the temperature span of 120–270 °C), enhanced H₂O tolerance with 6% H₂O (7% performance decrease) compared to non-methylated Mn-BTC (24% performance decrease), and more importantly, co-tolerance of H₂O and SO₂ is also enhanced (only 14% performance decrease) due to the improvement of the H₂O tolerance. Therefore, the influence of H₂O on NH₃ and NO adsorption in LT de-NO_x and the problem that ammonium bisulfate is difficult to decompose at low temperatures are solved. By integrating characterization and density functional theory (DFT) calculations, we shed light on the de-NO_x activity, the physicochemical structure of IPAx-Mn-BTC, and the reasons underlying the improved H₂O tolerance. We further explored the reaction mechanism using in-situ diffuse reflectance infrared Fourier transform spectroscopy (DRIFTS).

2. Experimental

2.1. Structures of IPAx-Mn-BTC

In order to ensure a good H₂O tolerance, different concentration of

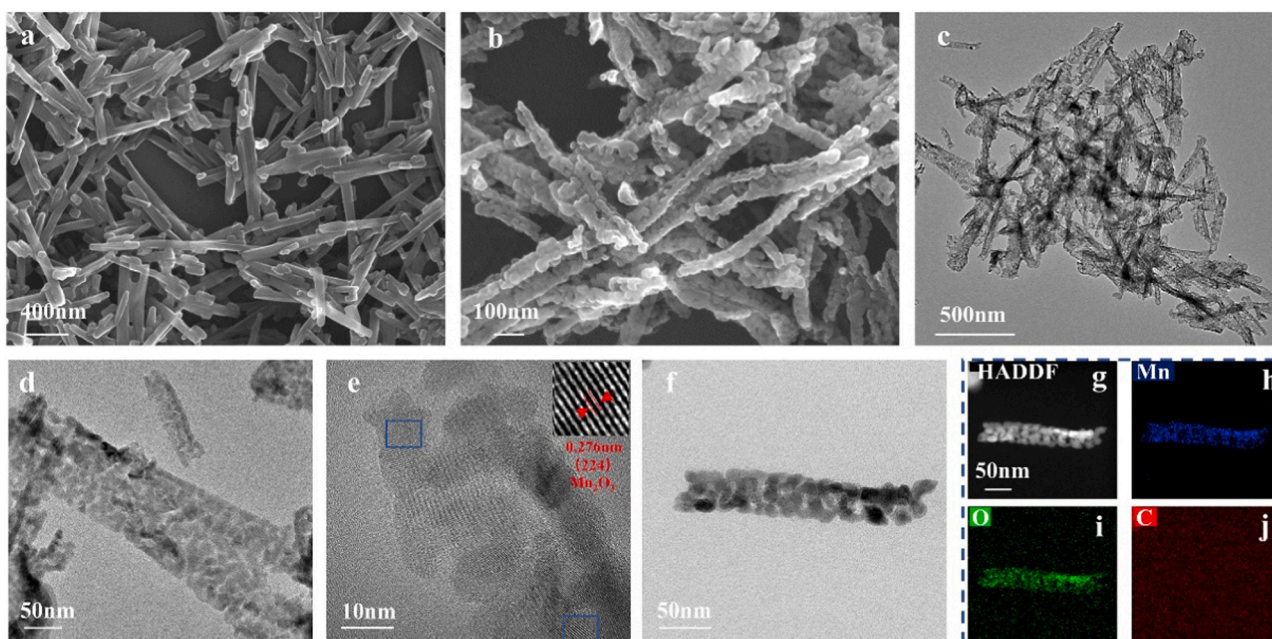


Fig. 2. SEM images of IPA50-Mn-BTC before (a) and after calcination (b); TEM images of IPA50-Mn-BTC (c-f); HAADF-STEM image (g) and the corresponding EDX elemental mappings (h-j) of IPA50-Mn-BTC.

IPA was introduced into Mn-BTC. 1230 mg of manganese acetate tetrahydrate and 3230 mg of trimesic acid were dissolved in 200 mL of solvent, which includes deionized water, ethanol, and isopropanol, with water and ethanol maintaining a volume ratio of 1:3. The six-coordinated Mn ions are connected with O to form MnO_6 octahedra, and the six octahedra are connected to each other to form clusters, and the clusters form a three-dimensional network structure through the ligand BTC [24]. During this process, IPA participates in the reaction, resulting in the combination of the hydrophobic functional group CH_3 in the Mn-BTC structure, as IPAx-Mn-BTC . 40, 50 and 60 mL of IPA were introduced, respectively, named IPA40-Mn-BTC, IPA50-Mn-BTC and IPA60-Mn-BTC. The mixed solution was stirred magnetically for 2 h at room temperature, and then carried out a hydrothermal reaction at 110 °C for 18 h. More details about the synthesis are in [supporting information](#) (Section 1). The physical and chemical structures of the IPAx-Mn-BTC were also analyzed in detail through characterizations (Section 2, [Supporting Information](#)).

2.2. Activity test

The activity of IPAx-Mn-BTC for the LT reduction of NO by NH_3 was explored with a simulated gas flow including 500 ppm NO, 500 ppm NH_3 , 5% O_2 , SO_2 (if needed), 6% H_2O (if needed) and N_2 as balance gas, more details are in [Section 3](#) of the [supporting information](#). The NO_x conversion, NH_3 conversion and N_2 selectivity were obtained using the follow [Eqs. \(1\), \(2\) and \(3\)](#).

$$\text{NO}_x\text{Conversion} = \frac{[\text{NO}_x]_{\text{in}} - [\text{NO}_x]_{\text{out}}}{[\text{NO}_x]_{\text{in}}} \times 100\% \quad (1)$$

$$\text{NH}_3\text{Conversion} = \frac{[\text{NH}_3]_{\text{in}} - [\text{NH}_3]_{\text{out}}}{[\text{NH}_3]_{\text{in}}} \times 100\% \quad (2)$$

$$\text{N}_2\text{Selectivity} = \left(1 - \frac{[\text{NO}_2]_{\text{out}} + 2[\text{N}_2\text{O}]_{\text{out}}}{([\text{NH}_3]_{\text{in}} + [\text{NO}_x]_{\text{in}}) - ([\text{NH}_3]_{\text{out}} + [\text{NO}_x]_{\text{out}})}\right) \times 100\% \quad (3)$$

Where, the subscripts “in” and “out” related to the inlet and outlet gas concentrations, respectively.

2.3. Mechanism analysis

In-situ DRIFTS was performed to explore the reaction mechanisms and the intermediates- H_2O was also introduced during the in-situ DRIFTS analysis to explore the effect of H_2O on the reaction mechanism and the formation of intermediates. Besides, the adsorption energy and the total density of states were analyzed by DFT calculation to further explain reaction mechanisms and the impact of methylation on structure and properties.

3. Results and discussion

3.1. Textural characteristic

The catalysts were synthesized by a hydrothermal method and subsequently subjected to a two-stage calcination before application ([Fig. 1a](#)). The thermal stability of the catalysts was analyzed through thermal gravimetric analysis (TGA, [Fig. 1b](#)), and it was found that the introduction of IPA enhanced the thermal stability. The mass decrease before about 170 °C is attributed to impurities and H_2O in the samples, and the decrease in the range of about 170–380 °C is the removal of OH group and the release of CO_2 from the trimesic ligand, forming a more stable structure, quasi-MOF [25,26]. Quasi-MOF is a structure between MOF and metal oxides obtained by stabilizing the MOF structure through N_2 calcination, and then removing part of the ligands through air calcination. This structure reduces the part of organic ligands, thereby weakening the carbonization process. The two-stage calcination treatment successfully enhanced the thermal stability of the catalyst, which is crucial in thermocatalysis. After the introduction of IPA, the crystal structure explored by powder x-ray diffraction (PXRD) of the catalyst did not change ([Fig. 1c](#)), the characteristic peak of Mn-BTC appeared before calcination, and the characteristic peak of Mn_2O_3 appeared after calcination. By analyzing the pore structure of the catalysts ([Fig. 1d](#) and [e](#), [Fig. S1](#) and [Table S1](#)), a discerning observation emerged that while the incorporation of IPA yielded a marginal reduction in the specific surface area and pore volume of the catalysts, these materials nonetheless maintained a characteristic type-IV isotherm profile[27,28], and the distinct hysteresis loop between the adsorption and desorption branches suggests the existence of mesopores, as also

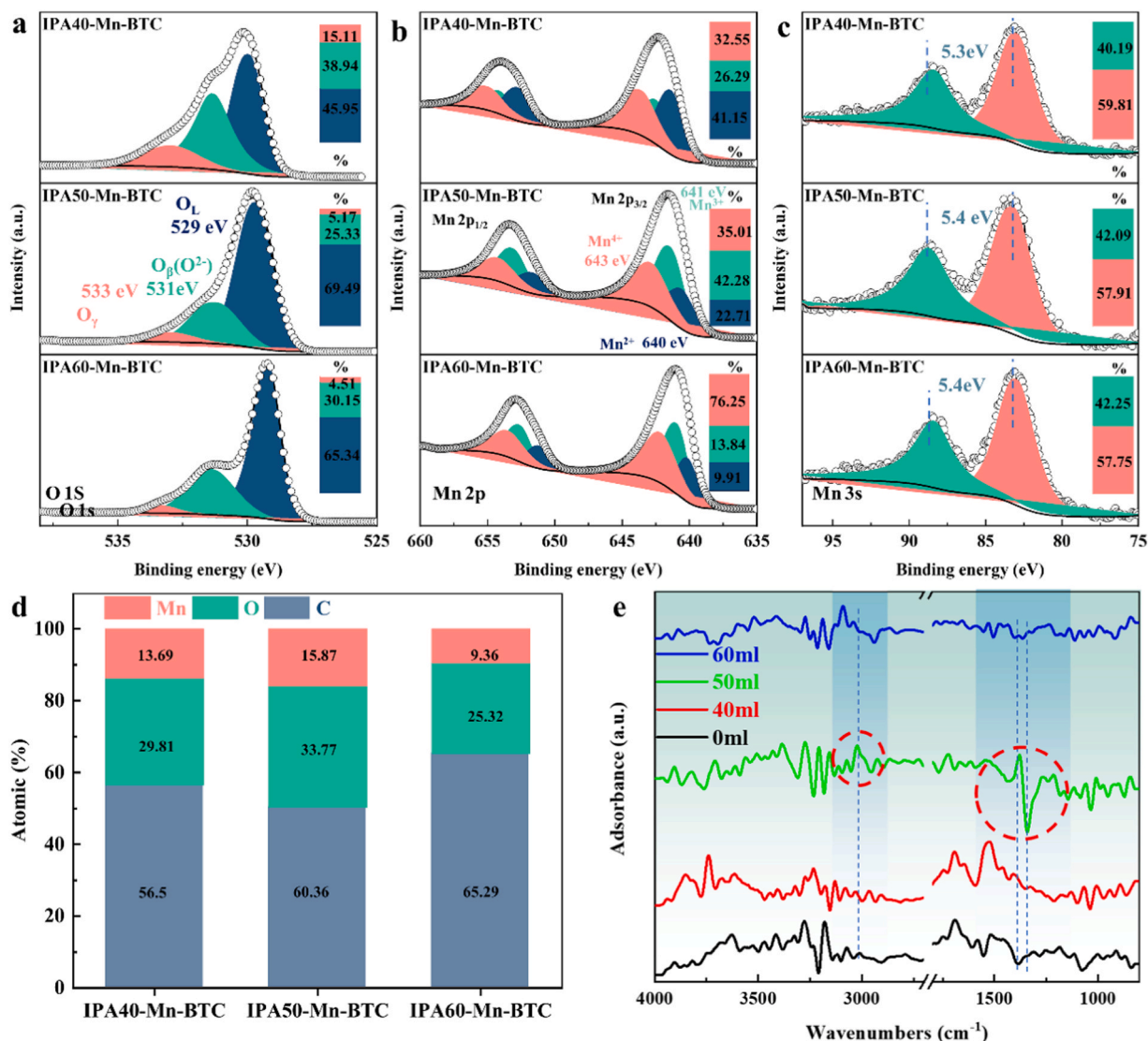


Fig. 3. Chemical characterization of catalysts: XPS spectra of IPAx-Mn-BTC in the O 1 s region (a), Mn 2p region (b) and Mn 3 s region (c); The element proportion of IPAx-Mn-BTC (d); DRIFT spectra of IPAx-Mn-BTC (e).

confirmed by the pore size distribution results. The presence of mesopores can reduce the mass loss during the mass transfer of adsorbate. Since the adsorption-desorption curves of the samples were similar, the curves were shifted on the y-axis, as shown in Fig. S1 for better analysis. Importantly, the introduction of IPA led to the notable shifts in the pore size distribution, especially for IPA50-Mn-BTC, the pores smaller than 4.3 nm disappeared compared with other samples. The augmentation in pore size weakens the capillary effect and prevents the adsorption and further diffusion of H₂O on the catalyst. Through the above analysis, it is believed that the introduction of IPA, that is, IPAx-Mn-BTC and Mn-BTC have the same structure, and IPA does not destroy the formation of MOF, but has an impact on the pore size. Whether the methyl functionalization is successful and the physicochemical structure of IPAx-Mn-BTC needs further analysis.

IPAx-Mn-BTC existed as nanorods before and after calcination (Fig. 2a-b and Fig. S2). However, a number of voids were generated after calcination, which is due to the removal of bound H₂O and CO₂ during the calcination process, while part of the ligands was also removed [29, 30]. While maintaining the nanorod structure, the pore structure is more abundant, exposing more active sites, and at the same time removing part of the C element that is easy to cause thermal aging of the catalyst. Transmission electron microscopy (TEM) (Fig. 2c-f), high-angle annular

dark-field scanning transmission electron microscopy (HAADF-STEM) and energy dispersive X-ray spectroscopy (EDX) mapping (Fig. 2g-j) were performed on IPA50-Mn-BTC to further explore the structure. The lattice (224) belonging to Mn₂O₃ was discerned (Fig. 2e), which provides evidence that during the heat treatment, Mn₂O₃ is indeed formed, aligning coherently with the patterns identified in PXRD [31,32].

X-ray photoelectron spectroscopy (XPS) and DRIFTS were explored to elucidate the chemical structure characteristics. In the C 1 s spectrum (Fig. S3) of IPAx-Mn-BTC, three distinguishable peaks were observed, which correspond to the C-H bond (284.8 eV), C-C bond (285.7 eV) and C=O bond (288.8 eV), respectively [33]. The increasing peak of C-C bond in IPA50-Mn-BTC implies that there are more methyl groups, and the C in the methyl group forms a bond with the C in the ligand. Turning to the O 1 s (Fig. 3a), three predominant peaks were identified: lattice oxygen (O_L, 529 eV) within MnO_x, surface active oxygen (O_β, 531 eV) and surface adsorbed oxygen (O_γ, 533 eV) [34]. Due to its low coordination features, which may originate from oxygen (V₀) or weakly bonded of surface oxygen species [35,36], O_β exhibits enhanced mobility at LT. The Mn 2p (Fig. 3b) could be fitted into six peaks, including Mn²⁺, Mn³⁺ and Mn⁴⁺ [37]. The increase of IPA resulted in the increase of Mn⁴⁺ and the decrease of Mn²⁺, Mn³⁺ increased first and then decreased and IPA50-Mn-BTC had the most Mn³⁺ content. Among

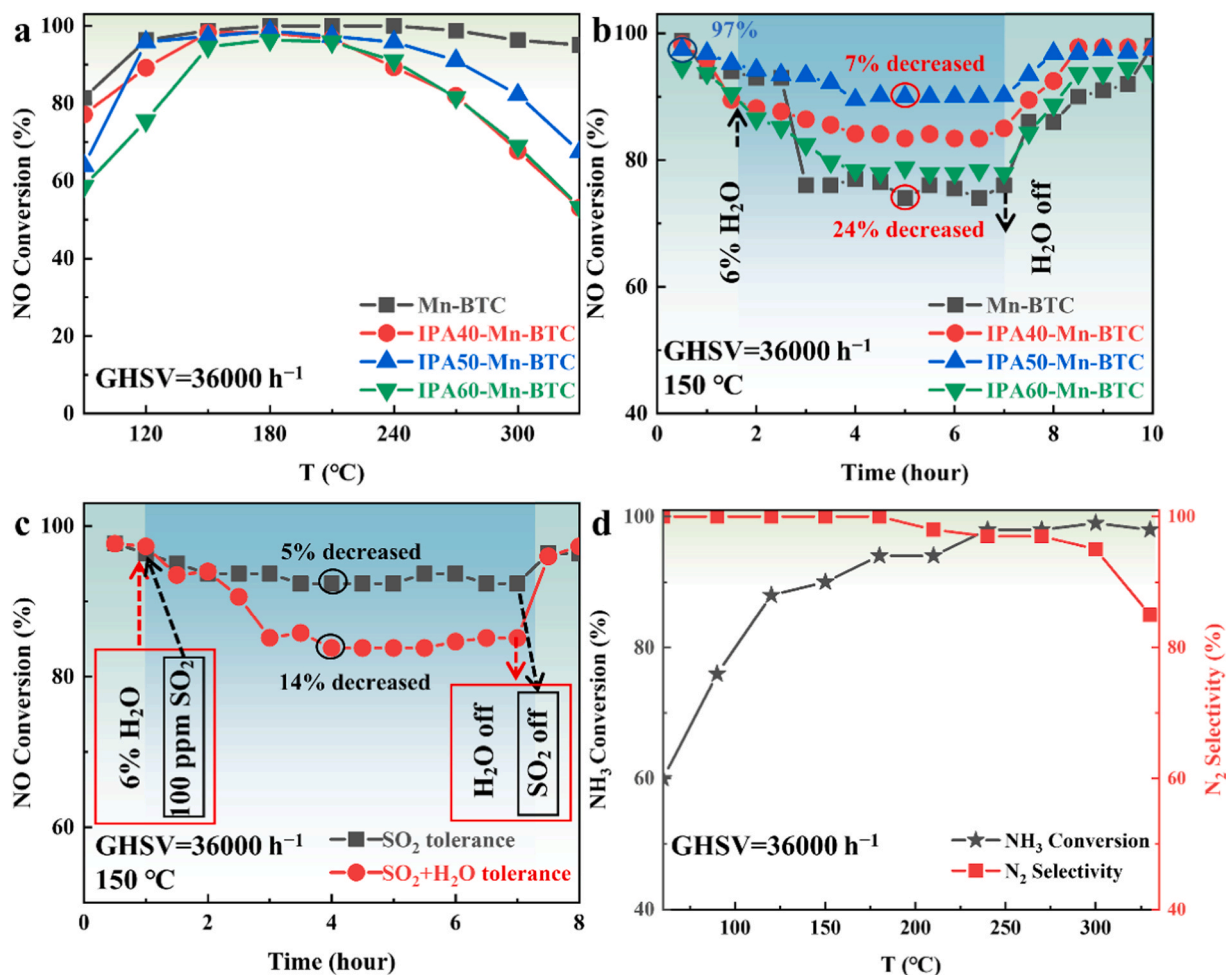


Fig. 4. NH₃-SCR activity: De-NO_x performance of the IPAx-Mn-BTC (a); The tolerance of 6% H₂O on the IPAx-Mn-BTC (b); The tolerance of 100 ppm SO₂ and the co-tolerance of 100 ppm SO₂ and 6% H₂O on the IPA50-Mn-BTC (c) N₂ selectivity and NH₃ conversion of IPA50-Mn-BTC (d).

them, Mn³⁺ species appear to bolster the V_o content and amplify the mobility of the bulk oxygen species. These factors together enhance the redox capacity, thereby promoting catalytic reaction. The Mn 3 s peak splitting can be attributed to the exchange coupling between the 3 s holes and 3d electrons of Mn. This peak splitting magnitude serves as a reliable metric for discerning the oxidation state of Mn: a range of 4.5–4.8 eV is indicative of MnO₂, 5.3–5.4 eV corresponds to Mn₂O₃, and 5.5–5.6 eV represents Mn₃O₄. The Mn 3 s splitting (Fig. 3c) indicating the oxidation state of Mn is Mn₂O₃, which is consistent with the results of PXRD and TEM [38,39]. For these three samples, IPA50-Mn-BTC had the most Mn content and O content, the least C element (Fig. 3d), which results the best thermal stability, and the most active ingredients. DRIFTS results (Fig. 3e) shows that IPA50-Mn-BTC had obvious methyl stretching vibration peak and methyl deformation vibration peaks, indicating that the methyl functionalization has been successfully realized [40,41]. In addition, the methyl peak of IPA50-Mn-BTC was more obvious than other samples, this is because the methyl content of IPA40-Mn-BTC is less, while the increase of IPA in the reaction process of IPA60-Mn-BTC leads to the decrease of ethanol and water, the reduction of solvent affects the growth of MOF. Furthermore, Raman spectra were used to study the V_o that can reduce the reaction energy barrier and promote molecular activation. There is an obvious peak attributed to V_o at 640 cm⁻¹ [21], and when the IPA is increased to 60 mL, the V_o decreases (Fig. S4). Whether IPAx-Mn-BTC can really improve the H₂O tolerance of the de-NO_x catalyst needs further performance testing.

3.2. Catalytic de-NO_x performance assessment

After adding IPA, the de-NO_x performance decreased compared with Mn-BTC, which was caused by the decrease of pore volume and specific surface area (Fig. 4a). However, among IPAx-Mn-BTC, IPA50-Mn-BTC can still maintain a good performance, which remained above 90% NO conversion between 120 and 270 °C at a gas hourly space velocity (GHSV) of 36,000 h⁻¹. By introducing 6% H₂O at 36,000 h⁻¹ and 150 °C to study the regulation of methyl functionalization on the H₂O tolerance (Fig. 4b). It can be found that the H₂O tolerance of the four samples had indeed improved, among which IPA50-Mn-BTC has improved the most, from a performance decrease of 24% in the presence of H₂O to a decrease of 7%, and the performance of continuous reaction for 6 h is still maintained at 90%. The reason for the best H₂O tolerance of IPA50-Mn-BTC compared with other samples is that it has the highest degree of methylation, and the small pore size (< 4.3 nm) disappeared. The enlargement of pore size poses a hindrance to the adsorption and diffusion of H₂O molecules on the surface of the catalyst, thereby leading to an enhancement in H₂O tolerance. Besides, the influence of H₂O on catalyst performance exhibits reversible, and the performance recovered immediately after removal of H₂O, which means that the existence of H₂O only competes with NH₃ or NO for adsorption, occupying some active sites, resulting in a slight decrease in performance, but not damaging the active sites. A small amount of SO₂ is also unavoidable in the flue gases, so 100 ppm SO₂ was introduced to analyze the SO₂ tolerance and simultaneous H₂O and SO₂ tolerance of the IPA50-Mn-BTC sample (Fig. 4c). The effects of H₂O and SO₂ on the catalyst were

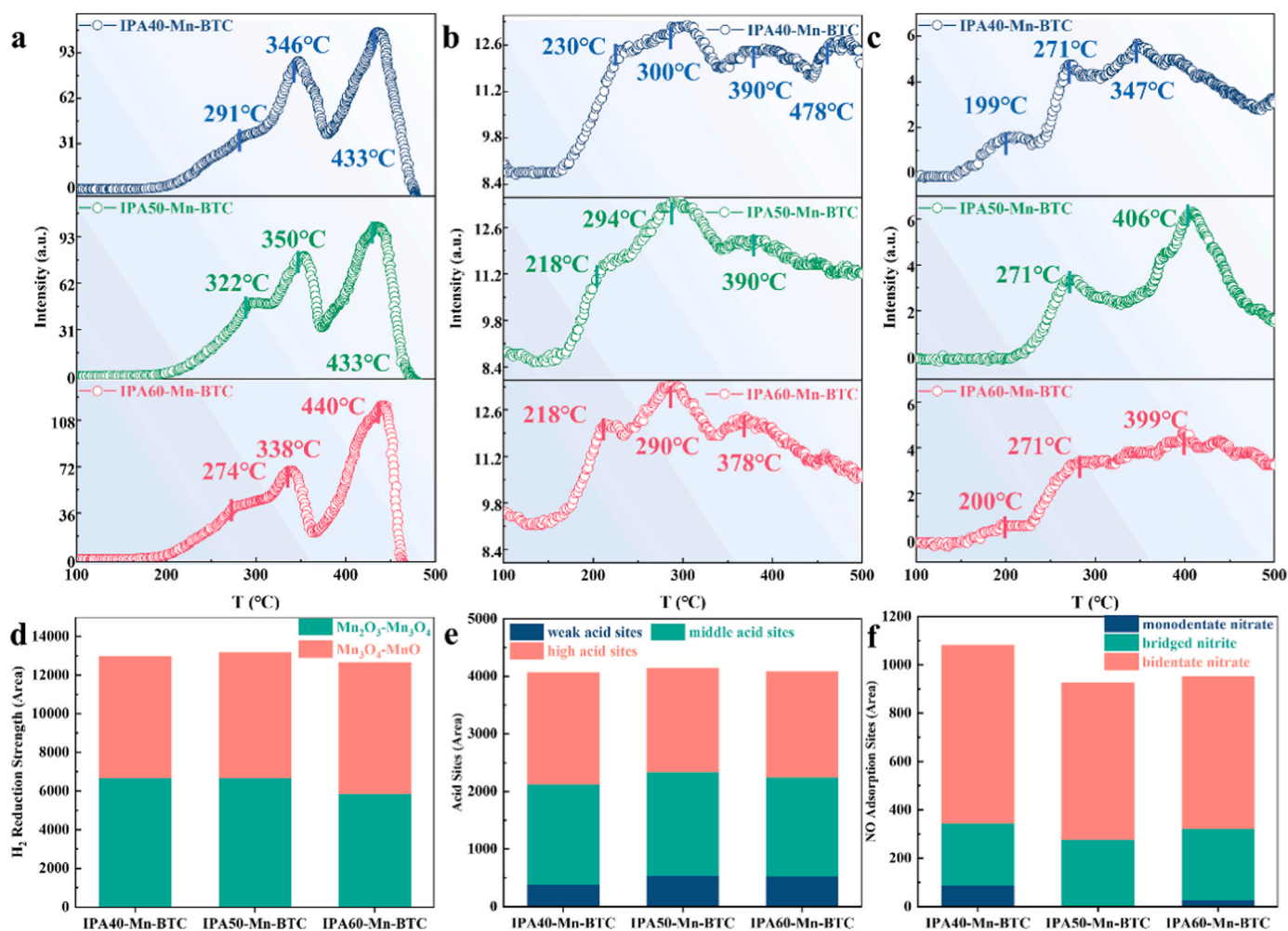


Fig. 5. H₂-TPR (a and d), NH₃-TPD (b and e), NO-TPD (c and f) over IPAx-Mn-BTC.

reversible, and the de-NO_x performance of the catalyst only dropped by 5% after the introduction of SO₂, which shows that the catalyst has both good H₂O and SO₂ tolerance. The co-tolerance of H₂O and SO₂ also improved compared with the catalyst without methyl functionalization (Fig. S5a). Nonetheless, this effect is reversible, negating the possibility of H₂O and SO₂ reacting with Mn to form sulfate species that could jeopardize active sites. Similarly, there is no reaction with NH₃ to generate ammonium sulfate that would accumulate on the surface of the catalyst. The NH₃ conversion and N₂ selectivity of IPA50-Mn-BTC were also analyzed (Fig. 4d). The NH₃ conversion was relatively low at LT because the lower performance before 120 °C results the escape of NH₃. N₂ selectivity decreased at higher temperatures because NH₃ was oxidized to generate N₂O, which is also the reason for activity decline after 300 °C. To further prove the thermal stability of IPA50-Mn-BTC, we conducted a de-NO_x activity test at 270 °C for 30 h (Fig. S5b) and found that there was basically no change in performance, indicating that the catalyst has excellent thermal stability. Moreover, the design of the quasi-MOF removes a large amount of C element during the calcination process, avoiding carbonization, which is also the reason for its good thermal stability. Combining the de-NO_x performance, H₂O and SO₂ tolerance, and N₂ selectivity of the IPA50-Mn-BTC, it can be found that the activity of IPA50-Mn-BTC is better than other similar structures reported in the literature (Table S2).

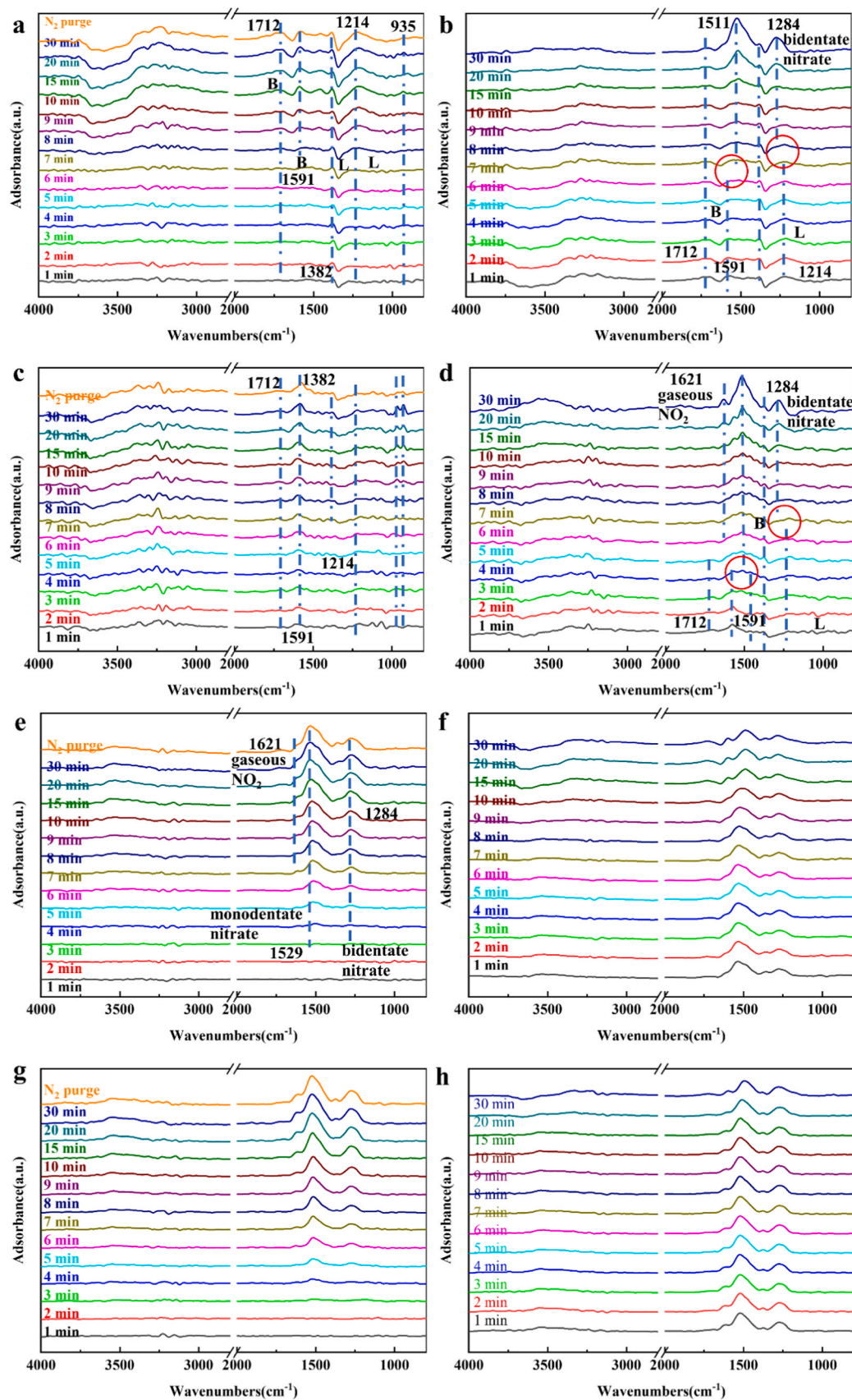
3.3. Adsorption sites and redox properties assessment

Redox and active sites are two important factors that determine the

de-NO_x performance. The utilization of H₂ temperature-programmed reduction (H₂-TPR) enabled an investigation into the redox properties of IPAx-Mn-BTC (Fig. 5a and d). Notably, three distinctive reduction peaks were observed. The first two peaks, occurring at lower temperature (<360 °C), were attributed to the reduction of Mn₂O₃ to Mn₃O₄, while the third peak within the 430–440 °C range signified the reduction of Mn₃O₄ to MnO[42–44]. Fig. 5d implies that IPA50-Mn-BTC has the strongest redox ability, which is why its de-NO_x performance is better than other samples. For an investigation into the adsorption behavior of NH₃ (Fig. 5b and e) and NO (Fig. 5c and f) on IPAx-Mn-BTC, NH₃ and NO temperature-programmed desorption (TPD) were conducted. The increase of IPA led to the shift of the desorption peak to the LT, which is beneficial to promote the occurrence of de-NO_x reaction. IPA50-Mn-BTC had the most adsorption sites, which is one of the reasons for its good de-NO_x performance. The results of NO-TPD indicated that the adsorption of IPAx-Mn-BTC for NO was significantly weaker than that for NH₃. IPA50-Mn-BTC had the fewest NO adsorption sites. The adsorption of NH₃ is the most important in the de-NO_x reaction, and the adsorption of NO is not the factor that determines the activity, but it will affect the reaction mechanism.

3.4. In-situ DRIFT analysis for de-NO_x mechanism

The catalytic reaction mechanism and the effect of H₂O on the reaction mechanism and intermediate states were explored by in-situ DRIFTS (Section 4, Supporting Information) over IPA50-Mn-BTC. Distinctive bands attributed to the adsorbed NH₃ species on Lewis (L)



(caption on next page)

Fig. 6. Dynamic evolution of the in-situ DRIFTS spectra for NH_3 adsorption (a) and under $\text{NO}+\text{O}_2$ flow following pre-exposure to NH_3 at 150°C on IPA50-Mn-BTC (b); Dynamic evolution of the in-situ DRIFTS spectra for NH_3 (c) and under $\text{NO}+\text{O}_2$ flow following pre-exposure to NH_3 at 150°C on IPA50-Mn-BTC (d) with the introduction of H_2O . Dynamic evolution of the in-situ DRIFTS spectra for $\text{NO}+\text{O}_2$ adsorption (e) and under NH_3 flow following pre-exposure to $\text{NO}+\text{O}_2$ at 150°C on IPA50-Mn-BTC (f); Dynamic evolution of the in-situ DRIFTS spectra for $\text{NO}+\text{O}_2$ adsorption (g) and under NH_3 flow following pre-exposure to $\text{NO}+\text{O}_2$ at 150°C on IPA50-Mn-BTC (h) with the introduction of H_2O .

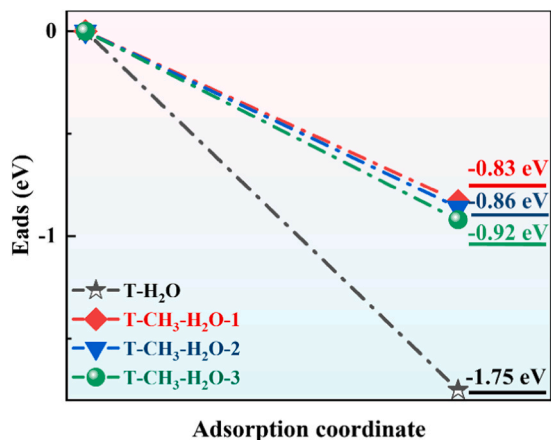


Fig. 7. The adsorption energies (eV) of H_2O on T and T-CH_3 clusters.

acid sites (1712 and 1591 cm^{-1}), the adsorbed NH_4^+ species on Brønsted (B) acid sites (1382 and 1214 cm^{-1}) and the weakly adsorbed NH_3 species at 935 cm^{-1} (Fig. 6a) appeared [45,46]. Then, an investigation

into the reactivity of pre-adsorption NH_3 with $\text{NO}+\text{O}_2$ was executed. The peaks of weakly adsorbed NH_3 and NH_3 at the L acid site disappeared, and the peak of NH_4^+ at the B acid site shifted, followed by the peak of bidentate nitrate (1284 cm^{-1}) after the introduction of $\text{NO}+\text{O}_2$ (Fig. 6b) [47,48]. It shows that the adsorbed NH_3 reacted with free NO , that is, there is an Eley-Rideal (E-R) reaction mechanism within the reaction pathway. The introduction of H_2O in the process of NH_3 adsorption (Fig. 6c) was observed to not hinder NH_3 adsorption, nor did it exert an inhibitory influence on the reaction involving $\text{NO}+\text{O}_2$ and pre-adsorbed NH_3 (Fig. 6d). Concurrently, the appearance of the NO_2 peak indicated a more efficient “Fast SCR” occurred during the E-R reaction. In addition to the E-R reaction, the Langmuir-Hinshelwood (L-H) reaction may occur during the SCR process, that is, the reaction of adsorbed NO and adsorbed NH_3 . Distinctive bands corresponding to gaseous NO_2 (1621 cm^{-1}), monodentate nitrate (1529 cm^{-1}) and bidentate nitrate (1284 cm^{-1}) appeared after the introduction of $\text{NO}+\text{O}_2$ (Fig. 6e) [49,50], implying IPA50-Mn-BTC could adsorb NO , aligning with the findings from NO -TPD analysis, and IPA50-Mn-BTC had a strong oxidizing ability, NO was oxidized to NO_2 during the adsorption process. However, it was found that there was no change in the peak after introducing NH_3 on the basis of pre-adsorbed $\text{NO}+\text{O}_2$ (Fig. 6f), indicating that NH_3 and pre-adsorbed NO did not react, there

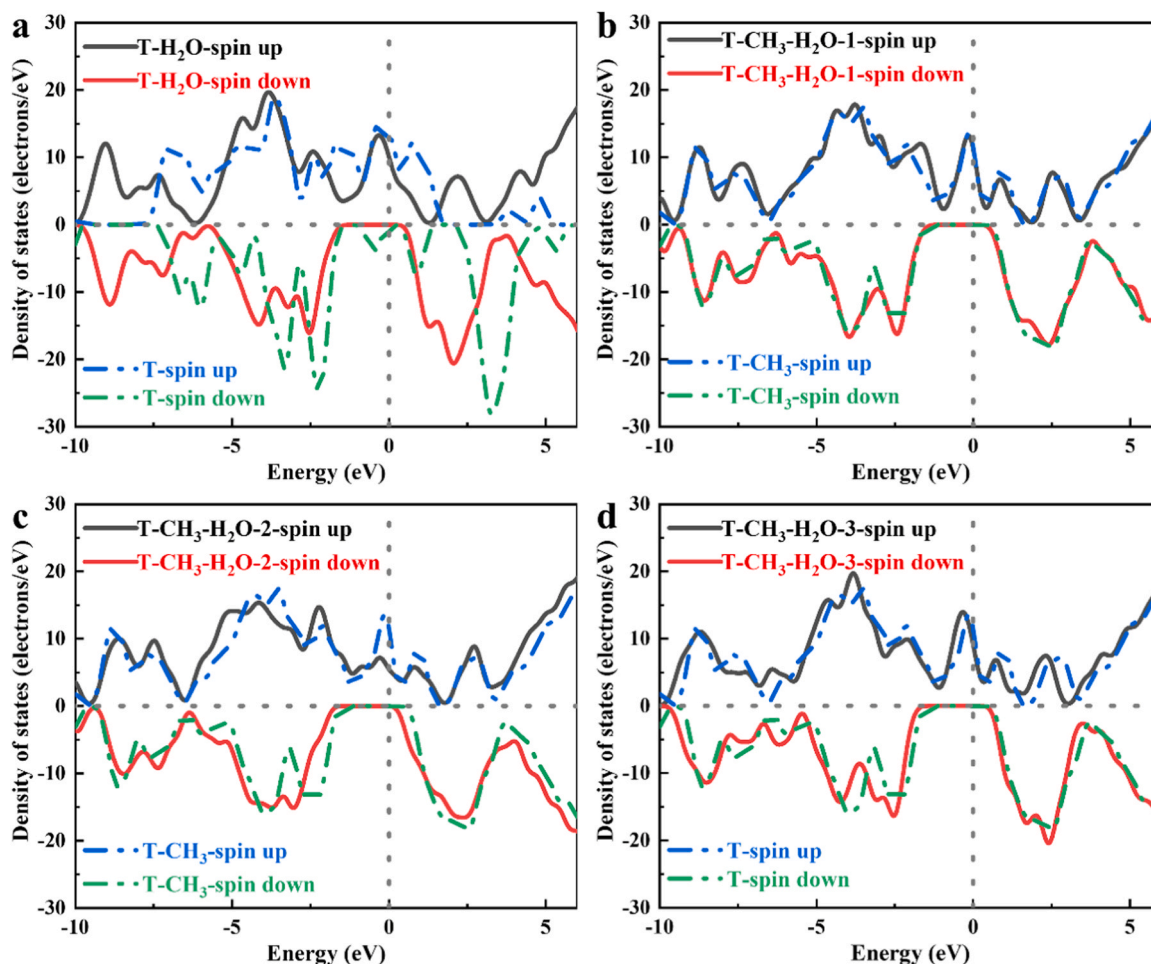


Fig. 8. TDOS before and after H_2O adsorption on T (a) and T-CH_3 (b-d).

was no L-H mechanism in the reaction process. Therefore, although the NO-TPD results show that the adsorption of NO by IPA50-Mn-BTC is weak, this does not affect the catalyst activity, and NO does not occupy the active sites, which will ensure more NH₃ adsorption. In addition, H₂O had no effect on the adsorption of NO (Fig. 6g) and did not promote the occurrence of L-H reaction (Fig. 6h). Overall, only the E-R reaction occurs, including “Standard SCR” and “Fast SCR”.

3.5. DFT calculations for de-NO_x mechanism

The geometrical optimization of methyl-functionalized (T-CH₃) and non-methyl-functionalized (T) clusters and the two clusters after adsorbing H₂O was carried out (Fig. S6), and the adsorption energy (Fig. 7) and electronic structure were analyzed to further reveal the reasons for the improvement of H₂O tolerance. For the T-CH₃, we designed three different morphologies for H₂O adsorbing. The adsorption energies of clusters after methylation are 0.83, 0.86 and 0.92 eV, respectively, and the adsorption energy of cluster without methylation is 1.75 eV, indicating that the design of methylation does reduce the adsorption capacity of the catalyst for H₂O and enhances the H₂O tolerance. By comparing the TDOS of the cluster and the cluster after adsorbing H₂O, it can be also found that the TDOS of the T-CH₃ has basically no change after absorbing H₂O (Fig. 8b-d), while significant shift was found after the T absorbed H₂O (Fig. 8a). The shift of TDOS is caused by the electron transfer between H₂O and active site, indicating that H₂O has a strong adsorption on T, but weakly on T-CH₃. Therefore, the design of methylation reduces the adsorption capacity of the catalyst for H₂O, who will not occupy the active sites, and will not compete with NH₃ and NO for adsorption, which ensures the excellent H₂O tolerance of the catalyst.

4. Conclusions

In exhaust gases with high H₂O content, de-NO_x catalysts are always succumbed to H₂O poisoning and subsequent deactivation. To address this issue, we meticulously engineered a series of IPA_x-Mn-BTC catalysts. Activity tests reveal that the methyl functionalization indeed enhances the H₂O tolerance of the catalysts. Specifically, IPA50-Mn-BTC exhibits a NO conversion above 90% between 120 and 270 °C at a GHSV of 36,000 h⁻¹, with H₂O tolerance evident as only a 7% NO conversion decreases at 150 °C. Impressively, the catalyst also guarantees reliable SO₂ tolerance with only a 5% NO conversion decreases by 100 ppm SO₂ introducing at 150 °C. The hydrophobic methyl functional group plays a key role in improved H₂O tolerance. Upon functionalization in IPA50-Mn-BTC, pore size under 4.3 nm are disappeared, thereby impeding H₂O adsorption and diffusion on the catalyst surface and favoring improved H₂O tolerance. Evaluations of adsorption energy and TDOS further indicate diminished H₂O adsorption following methyl functionalization. The design of the LT de-NO_x catalyst circumvents energy wastage associated with reheating flue gases for de-NO_x, and simultaneously bolsters the efficiency of flue gases treatment in emissions with high H₂O content. Concurrently, it also ensures good SO₂ tolerance, allowing the catalyst to use in multi-environment waste gases containing H₂O or SO₂. Overall, this research pioneers an innovative approach to controlling industrial NO_x emissions with pronounced H₂O content at LT, offering insights for the formulation of sophisticated LT de-NO_x catalysts.

CRedit authorship contribution statement

Kunli Song: Writing – original draft, Conceptualization, Investigation. **Jiyuan Hu:** Investigation. **Peng Lu:** Resources. **Dandan Ma:** Methodology. **Xinya Zhou:** Data curation. **Jun Li:** Validation. **Ting Jiang:** Visualization. **Lu Li:** Formal analysis. **Shangyuan Wu:** Formal analysis. **Jian-Wen Shi:** Conceptualization, Methodology, Writing – review & editing, Funding acquisition.

Declaration of Competing Interest

The authors declare that they have no known competing financial interests or personal relationships that could have appeared to influence the work reported in this paper.

Data Availability

Data will be made available on request.

Acknowledgements

This work was supported by the National Natural Science Foundation of China (21972110), the Guangdong Province Engineering Laboratory for Air Pollution Control (No. 20193236-09-04), the State Key Laboratory of Electrical Insulation and Power Equipment (EIP23315), and the Fundamental Research Funds for the Central Universities (xtr062023001). XPS and TEM were measured at Analysis and Test Center of Xi'an Jiaotong University, and we thank Miss Jiamei Liu for her assistance in the measurements.

Appendix A. Supporting information

Supplementary data associated with this article can be found in the online version at doi:10.1016/j.apcatb.2023.123548.

References

- [1] L.E. Gevers, L.R. Enakonda, A. Shahid, S. Ould-Chikh, C.I. Silva, P.P. Paalanen, A. Aguilar-Tapia, J.-L. Hazemann, M.N. Hedhili, F. Wen, Unraveling the structure and role of Mn and Ce for NO_x reduction in application-relevant catalysts, *Nat. Commun.* 13 (2022) 2960.
- [2] W. Hu, F. Gramigni, N.D. Nasello, N. Usberti, U. Iacobone, S. Liu, I. Nova, X. Gao, E. Tronconi, Dynamic binuclear CuII sites in the reduction half-cycle of low-temperature NH₃-SCR over Cu-CHA catalysts, *ACS Catal.* 12 (2022) 5263–5274.
- [3] Z. Zhang, J. Ye, D. Tan, Z. Feng, J. Luo, Y. Tan, Y. Huang, The effects of Fe₂O₃ based DOC and SCR catalyst on the combustion and emission characteristics of a diesel engine fueled with biodiesel, *Fuel* 290 (2021), 120039.
- [4] Y. Wan, W. Zhao, Y. Tang, L. Li, H. Wang, Y. Cui, J. Gu, Y. Li, J. Shi, Ni-Mn bi-metal oxide catalysts for the low temperature SCR removal of NO with NH₃, *Appl. Catal. B* 148 (2014) 114–122.
- [5] G. Qi, R.T. Yang, Performance and kinetics study for low-temperature SCR of NO with NH₃ over MnO_x-CeO₂ catalyst, *J. Catal.* 217 (2003) 434–441.
- [6] M. Casapu, O. Kröcher, M. Elsener, Screening of doped MnO_x-CeO₂ catalysts for low-temperature NO-SCR, *Appl. Catal. B* 88 (2009) 413–419.
- [7] Z. Zhang, J. Li, J. Tian, Y. Zhong, Z. Zou, R. Dong, S. Gao, W. Xu, D. Tan, The effects of Mn-based catalysts on the selective catalytic reduction of NO_x with NH₃ at low temperature: a review, *Fuel Process. Technol.* 230 (2022), 107213.
- [8] L. Zhang, D. Wang, Y. Liu, K. Kamasamudram, J. Li, W. Epling, SO₂ poisoning impact on the NH₃-SCR reaction over a commercial Cu-SAPO-34 SCR catalyst, *Appl. Catal. B* 156 (2014) 371–377.
- [9] B. Wang, M. Wang, L. Han, Y. Hou, W. Bao, C. Zhang, G. Feng, L. Chang, Z. Huang, J. Wang, Improved activity and SO₂ resistance by Sm-modulated redox of MnCeSmTiO_x mesoporous amorphous oxides for low-temperature NH₃-SCR of NO, *ACS Catal.* 10 (2020) 9034–9045.
- [10] R. Freund, O. Zaremba, G. Arnauts, R. Ameloot, G. Skorupskii, M. Dincă, A. Bavykina, J. Gascon, A. Ejsmont, J. Goscińska, The current status of MOF and COF applications, *Angew. Chem. Int. Ed.* 60 (2021) 23975–24001.
- [11] Q. Wang, D. Astruc, State of the art and prospects in metal-organic framework (MOF)-based and MOF-derived nanocatalysis, *Chem. Rev.* 120 (2019) 1438–1511.
- [12] J. Tang, Y. Yamauchi, MOF morphologies in control, *Nat. Chem.* 8 (2016) 638–639.
- [13] X. Ma, H. Liu, W. Yang, G. Mao, L. Zheng, H.-L. Jiang, Modulating coordination environment of single-atom catalysts and their proximity to photosensitive units for boosting MOF, *Photocatal., J. Am. Chem. Soc.* 143 (2021) 12220–12229.
- [14] A. Dhakshinamoorthy, A.M. Asiri, H. Garcia, Metal-organic framework (MOF) compounds: photocatalysts for redox reactions and solar fuel production, *Angew. Chem. Int. Ed.* 55 (2016) 5414–5445.
- [15] J. Liu, D. Zhu, C. Guo, A. Vasileff, S.Z. Qiao, Design strategies toward advanced MOF-derived electrocatalysts for energy-conversion reactions, *Adv. Energy Mater.* 7 (2017) 1700518.
- [16] C. Cao, D.D. Ma, Q. Xu, X.T. Wu, Q.L. Zhu, Semisacrificial template growth of self-supporting MOF nanocomposite electrode for efficient electrocatalytic water oxidation, *Adv. Funct. Mater.* 29 (2019) 1807418.
- [17] H. Jiang, J. Zhou, C. Wang, Y. Li, Y. Chen, M. Zhang, Effect of cosolvent and temperature on the structures and properties of Cu-MOF-74 in low-temperature NH₃-SCR, *Ind. Eng. Chem. Res.* 56 (2017) 3542–3550.

- [18] Y. Liu, J. Zhao, J.M. Lee, Conventional and new materials for selective catalytic reduction (SCR) of NO_x, *ChemCatChem* 10 (2018) 1499–1511.
- [19] S. Xie, Q. Qin, H. Liu, L. Jin, X. Wei, J. Liu, X. Liu, Y. Yao, L. Dong, B. Li, MOF-74-M (M = Mn, Co, Ni, Zn, MnCo, MnNi, and MnZn) for low-temperature NH₃-SCR and in situ DRIFTS study reaction mechanism, *ACS Appl. Mater. Interfaces* 12 (2020) 48476–48485.
- [20] Q. Zhou, K. He, X. Wang, K.H. Lim, P. Liu, W. Wang, Q. Wang, Investigation on the redox/acidic features of bimetallic MOF-derived CeMO_x catalysts for low-temperature NH₃-SCR of NO_x, *Appl. Catal. A-Gen.* 643 (2022), 118796.
- [21] K. Song, K. Guo, S. Mao, D. Ma, Y. Lv, C. He, H. Wang, Y. Cheng, J.-W. Shi, Insight into the origin of excellent SO₂ tolerance and de-NO_x performance of quasi-Mn-BTC in the low-temperature catalytic reduction of nitrogen oxide, *ACS Catal.* 13 (2023) 5020–5032.
- [22] S. Li, Y. Huang, H. Zhu, J. Long, L. Xiao, P. Li, L. Zhao, J. Zhang, Dual improvement in acid and redox properties of the FeO_x/OAC catalyst via APS oxygen-functionalization: High low-temperature NH₃-SCR activity, SO₂ and H₂O tolerance, *Fuel* 341 (2023), 127716.
- [23] Z. Jin, L. Wang, Q. Hu, L. Zhang, S. Xu, X. Dong, X. Gao, R. Ma, X. Meng, F.-S. Xiao, Hydrophobic zeolite containing Titania particles as wettability-selective catalyst for formaldehyde removal, *ACS Catal.* 8 (2018) 5250–5254.
- [24] Y. Fu, J. Su, S. Yang, G. Li, F. Liao, M. Xiong, J. Lin, Syntheses, structures and magnetic properties of Mn (II), Co (II) and Ni (II) metal-organic frameworks constructed from 1, 3, 5-benzenetricarboxylate and formate ligands, *Inorg. Chim. Acta* 363 (2010) 645–652.
- [25] Y. Zhang, L. Zhao, J. Duan, S. Bi, Insights into deNO_x processing over Ce-modified Cu-BTC catalysts for the CO-SCR reaction at low temperature by in situ DRIFTS, *Sep. Purif. Technol.* 234 (2020), 116081.
- [26] F. Gao, X. Tang, H. Yi, J. Li, S. Zhao, J. Wang, C. Chu, C. Li, Promotional mechanisms of activity and SO₂ tolerance of Co-or Ni-doped MnO_x-CeO₂ catalysts for SCR of NO_x with NH₃ at low temperature, *Chem. Eng. J.* 317 (2017) 20–31.
- [27] B. Shen, Y. Wang, F. Wang, T. Liu, The effect of Ce–Zr on NH₃-SCR activity over MnO_x (0.6)/Ce_{0.5}Zr_{0.5}O₂ at low temperature, *Chem. Eng. J.* 236 (2014) 171–180.
- [28] H.H. Phil, M.P. Reddy, P.A. Kumar, L.K. Ju, J.S. Hyo, SO₂ resistant antimony promoted V₂O₅/TiO₂ catalyst for NH₃-SCR of NO_x at low temperatures, *Appl. Catal. B* 78 (2008) 301–308.
- [29] N. Tsumori, L. Chen, Q. Wang, Q.-L. Zhu, M. Kitta, Q. Xu, Quasi-MOF: exposing inorganic nodes to guest metal nanoparticles for drastically enhanced catalytic activity, *Chem* 4 (2018) 845–856.
- [30] D. Luo, C. Li, Y. Zhang, Q. Ma, C. Ma, Y. Nie, M. Li, X. Weng, R. Huang, Y. Zhao, Design of quasi-MOF nanospheres as a dynamic electrocatalyst toward accelerated sulfur reduction reaction for high-performance lithium–sulfur batteries, *Adv. Mater.* 34 (2022) 2105541.
- [31] F. Jiao, A. Harrison, A.H. Hill, P.G. Bruce, Mesoporous Mn₂O₃ and Mn₃O₄ with crystalline walls, *Adv. Mater.* 19 (2007) 4063–4066.
- [32] Y.G. Zhang, J. Chen, B.J. Huang, D.P. Li, Fabrication of Mn₂O₃ nanorods and their different paramagnetic properties, *Adv. Mat. Res* 233 (2011) 2252–2257.
- [33] T. Cui, L. Li, C. Ye, X. Li, C. Liu, S. Zhu, W. Chen, D. Wang, Heterogeneous single atom environmental catalysis: fundamentals, applications, and opportunities, *Adv. Funct. Mater.* 32 (2022), 2108381.
- [34] Z. Ge, Y. Ding, X. Huang, Y. Shen, Mechanism of iron doping promoting high temperature deNO_x and anti-water vapor and SO₂ poisoning of ZrW (Fe) O_x, *Fuel* 332 (2023), 126248.
- [35] H. Nesbitt, D. Banerjee, Interpretation of XPS Mn (2p) spectra of Mn oxyhydroxides and constraints on the mechanism of MnO₂ precipitation, *Am. Mineral.* 83 (1998) 305–315.
- [36] C. Chen, Z.J. Tang, J.Y. Li, C.Y. Du, T. Ouyang, K. Xiao, Z.Q. Liu, MnO enabling highly efficient and stable Co-N_x/C for oxygen reduction reaction in both acidic and alkaline media, *Adv. Funct. Mater.* 33 (2023) 2210143.
- [37] Z. Zhang, J. Tian, J. Li, C. Cao, S. Wang, J. Lv, W. Zheng, D. Tan, The development of diesel oxidation catalysts and the effect of sulfur dioxide on catalysts of metal-based diesel oxidation catalysts: a review, *Fuel Process. Technol.* 233 (2022), 107317.
- [38] B.J. Tan, K.J. Klabunde, P.M. Sherwood, XPS studies of solvated metal atom dispersed (SMAD) catalysts. Evidence for layered cobalt-manganese particles on alumina and silica, *J. Am. Chem. Soc.* 113 (1991) 855–861.
- [39] S. Yao, S. Wang, R. Liu, X. Liu, Z. Fu, D. Wang, H. Hao, Z. Yang, Y.-M. Yan, Delocalizing the d-electrons spin states of Mn site in MnO₂ for anion-intercalation energy storage, *Nano Energy* 99 (2022), 107391.
- [40] M.B. Leonard, T. Li, M.J. Kramer, S.M. McDonnell, A.N. Vedernikov, E. Rodriguez, Spectroscopic studies of methyl paraoxon decomposition over mesoporous Ce-doped titanias for toxic chemical filtration, *J. Hazard. Mater.* 438 (2022), 129536.
- [41] S. Sun, N.F. Dummer, T. Bere, A.J. Barnes, G. Shaw, M. Douthwaite, S. Pattison, R. J. Lewis, N. Richards, D.J. Morgan, Selective oxidation of methane to methanol and methyl hydroperoxide over palladium modified MoO₃ photocatalyst under ambient conditions, *Catal. Sci. Technol.* 12 (2022) 3727–3736.
- [42] P. Pal, S. Saravanamurugan, Enhanced basicity of MnO_x-supported Ru for the selective oxidation of 5-hydroxymethylfurfural to 2, 5-furandicarboxylic acid, *ChemSusChem* 15 (2022), e202200902.
- [43] C. Fang, D. Zhang, S. Cai, L. Zhang, L. Huang, H. Li, P. Maitarad, L. Shi, R. Gao, J. Zhang, Low-temperature selective catalytic reduction of NO with NH₃ over nanoflake MnO_x on carbon nanotubes in situ prepared via a chemical bath deposition route, *Nanoscale* 5 (2013) 9199–9207.
- [44] D. Delimaris, T. Ioannides, VOC oxidation over MnO_x-CeO₂ catalysts prepared by a combustion method, *Appl. Catal. B* 84 (2008) 303–312.
- [45] B. Jiang, Z. Li, S.-c. Lee, Mechanism study of the promotional effect of O₂ on low-temperature SCR reaction on Fe–Mn/TiO₂ by DRIFT, *Chem. Eng. J.* 225 (2013) 52–58.
- [46] L. Wei, S. Cui, H. Guo, X. Ma, L. Zhang, DRIFT and DFT study of cerium addition on SO₂ of manganese-based catalysts for low temperature SCR, *J. Mol. Catal. A: Chem.* 421 (2016) 102–108.
- [47] S. Tamm, N. Vallim, M. Skoglundh, L. Olsson, The influence of hydrogen on the stability of nitrates during H₂-assisted SCR over Ag/Al₂O₃ catalysts—a DRIFT study, *J. Catal.* 307 (2013) 153–161.
- [48] D. Wang, Y. Peng, S.-c Xiong, B. Li, L.-n Gan, C.-m Lu, J.-j Chen, Y.-l Ma, J.-h Li, De-reducibility mechanism of titanium on maghemite catalysts for the SCR reaction: an in situ DRIFTS and quantitative kinetics study, *Appl. Catal. B* 221 (2018) 556–564.
- [49] J. Fan, P. Ning, Z. Song, X. Liu, L. Wang, J. Wang, H. Wang, K. Long, Q. Zhang, Mechanistic aspects of NH₃-SCR reaction over CeO₂/TiO₂-ZrO₂-SO₄2– catalyst: in situ DRIFTS investigation, *Chem. Eng. J.* 334 (2018) 855–863.
- [50] L. Ma, Y. Cheng, G. Cavataio, R.W. McCabe, L. Fu, J. Li, In situ DRIFTS and temperature-programmed technology study on NH₃-SCR of NO_x over Cu-SSZ-13 and Cu-SAPO-34 catalysts, *Appl. Catal. B* 156 (2014) 428–437.